



Effect of Variable Specific Energy Laser Remelting on the Morphology, Microstructure, and Mechanical Properties of Ta/Ni-Based Composite Coatings

JIANGTONG YU,^{1,2} WENLEI SUN,^{1,3} GUAN ZHANG,¹
QUANWEI CUI,¹ and HUACHAO JIAO¹

1.—School of Mechanical Engineering, Xinjiang University, Urumqi 830017, China.
2.—e-mail: yujtong@163.com. 3.—e-mail: sunwenxj@163.com

In this study, laser remelting was used to prepare Ta/Ni-based composite coatings using a combination of Ta-doping in a Ni-based powder. The effects of laser remelting specific energy and Ta-doping content on the surface morphology, phase composition, microstructure, bonding interface, microhardness, and wear resistance of the cladding layers were investigated. The unmelted powder particles on the coating surface disappeared after laser remelting. Laser remelting significantly decreased the grain size of the Ta/Ni-based composite coating, and the bright white microstructure of the doped Ta hindered crystal growth. With increase in the specific energy of the remelts, the internal porosity of the coating significantly decreased, overall grain size of the upper part of the composite coating gradually increased, central columnar crystal content gradually increased, overall crystal size of the lower part first decreased and then increased, and Ta and Ni diffused more fully at the bonding interface between the matrix and the coating, which decreased the difference in the chemical composition of the two sides of the bonding interface. The Ta/Ni-based composite remelted layers had significantly improved microhardness and wear resistance compared to before remelting, and both these parameters tended to increase and then decrease with increasing remelting specific energy.

INTRODUCTION

Laser cladding is a type of additive manufacturing technology.¹ It is advantageous because it forms a metallurgical bond between the substrate and the cladding layer^{2–4} and enables control of cladding layer composition,^{5,6} substrate dilution rate,^{7–9} and easy automation.¹⁰ It is widely used in fields such as aerospace, machinery,² petroleum,¹¹ and chemistry.^{12–14} Ni-Based alloy coatings are popular because of their good high-temperature resistance^{15,16} and corrosion resistance,¹⁷ however, the susceptibility to defects,^{18,19} stress,²⁰ and deformation problems^{21,22} during the preparation of high-performance Ni-based coatings by laser cladding is a

bottleneck that limits their development. Ta is a refractory metal²³ that readily reacts with carbon at suitable temperatures to produce high-hardness carbides.²⁴ Numerous researchers have worked on improving the performance of Ni-based cladding layers by adding other powders to the Ni-based powder;^{17,25–28} however, once the proportion of other powders reaches the optimal content for performance, the purpose of improving the comprehensive performance of the cladding layer without losing its original characteristics may not be achieved. To address the shortcomings of additive manufacturing, hybrid additive manufacturing uses a combination of additive manufacturing along with the advantages of other manufacturing technologies.^{29–34} Laser remelting is a surface modification technique that uses a high-energy laser beam of a certain specific energy to rapidly melt and solidify the surface of a workpiece.³⁵ Laser remelting can

(Received November 22, 2022; accepted March 13, 2023;
published online April 20, 2023)

address the defects,³⁶ such as cracks^{37,38} and pores,^{37,39–41} that are easily produced during the additive manufacturing of specific metal materials, to some extent, and it can improve the mechanical properties of the cladding layer.^{42,43} Thus, more researchers should investigate how hybrid additive manufacturing can be used to prepare defect-free, high-performance metal-based composite coatings with high surface flatness by using disposable clamping for substrates and in-line regulation.

In this study, laser remelting of a composite coating was carried out using various laser specific energy values on a composite Ta/Ni-based coating via laser cladding. The surface morphology, phase composition, microstructure, elemental distribution, microhardness, and wear resistance of the composite coatings were analyzed for different laser specific energy values. The hardness and wear resistance of the composite coatings before and after laser remelting were compared. The findings of this study provide insights for using hybrid additive manufacturing with a combination of laser cladding and laser remelting to fabricate Ni-based composite coatings.

EXPERIMENTAL PROCEDURE

Experimental Sample Preparation

During sample preparation, a 45 steel specimen (dimensions: 110 mm × 60 mm × 6 mm) was used as the substrate, and a total of five specimens were used. Before experiments, the surface of each substrate was polished to obtain a flat surface, and it was cleaned with alcohol and dried. Ni-based powder was provided by Jiano Metal Material Company, Nangong, China. The Ni-based self-fusing alloy powder had spherical particles with sizes in the range of 45–106 μm. The chemical composition of the Ni-based powder is presented in Table I. The mass fraction of the high-purity Ta powder was ≥ 99.95%, and the particle size was < 38 μm. A planetary ball mill type KQM-Z/B was used to mix the powder at a set rotational speed of 300 rpm, with the direction of rotation changing every 15 min, for a total of 2 h. The Ni-based and Ta powders were mixed, and the composition of the cladding powder for samples 1–5 is shown in Table II. The Ni-based and mixed powders were dried using an electric blast drying oven at 120 °C for 2 h. The results of mixing tantalum powder and nickel-based powder are shown in Fig. 1.

For the laser cladding experiment, a KUKA six-degree-of-freedom robot loaded with a YLS-2000

fiber laser system was used. The powder was fed in a synchronous coaxial manner, and argon was used as a protective gas. Multi-lap cladding process experiments were carried out on samples 1–5 using laser power (P) of 1400 W, scanning speed (V) of 4 mm/s, powder feed rate of 8.39 g/min, and overlap rate of 50%. To comprehensively study the effects of P , V , and spot diameter (D) of laser remelting on the microstructure and mechanical properties of composite coatings prepared from mixed powders, the specific energy (Eq. 1) was used to calculate the approximate magnitude of remelting energy per unit area:^{44,45}

$$E = \frac{P}{DV} \quad (1)$$

where E is the specific energy of the laser (J/mm²). Three-laser cladding samples prepared from mixed powders were remelted using various values of laser remelting specific energy (remelting without any metal powder added). The laser remelting parameters are shown in Table II.

Experimental Analysis Methods

The microstructure and property test samples were prepared by cutting the cladding layer using an electric discharge machining wire-cut machine. The cladding samples were ground with metallographic sandpapers with different mesh numbers, polished with a polishing machine, and then etched with aqua regia. Microstructures of the cladding samples were observed using field emission scanning electron microscopy (SEM, Quanta FEG 250), and chemical compositions and elemental distribution were analyzed using energy-dispersive spectrometry (EDS). X-ray diffraction (XRD) was used to analyze the phase compositions of the cladding layers. Surface morphology of the laser cladding and remelted layers was analyzed using a VHX-6000 super-depth field microscope. To study the effect of various remelting specific energies on the mechanical properties of the cladding layer, the microhardness (HXD-1000TB microhardness tester) and wear resistance (M-2000 wear tester) of the cladding layer of each sample were tested. Microhardness was tested with a loading force of 0.2 kgf and a loading time of 15 s, vertically from the top of the cladding to the substrate, at 0.2 mm intervals. To conduct dry wear tests, the cladding layer was loaded with a load of 130 N, and the speed was set to 180 rpm. The wear time was 60 min. An electronic digital balance was used to weigh each sample before and after loading for wear resistance analysis.

RESULTS AND DISCUSSION

Surface Morphology of the Cladding Layer

During laser cladding manufacturing, the parameters of the cladding process and the overlap rate

Table I. Chemical composition of the Ni-based powder (wt.%)

c	Cr	Si	B	Fe	Ni
0.5–1.0	14–19	3.5–5.0	3.0–4.5	< 8.0	Bal

Table II. Cladding powder composition and laser remelting parameters of samples 1–5

Powder and remelting process	Sample 1	Sample 2	Sample 3	Sample 4	Sample 5
Ni-Based powder (g)	100	94	94	94	94
Ta powder (g)	0	6	6	6	6
Remelting specific energy E/(J/mm ²)	–	–	20.83	38.89	75.00

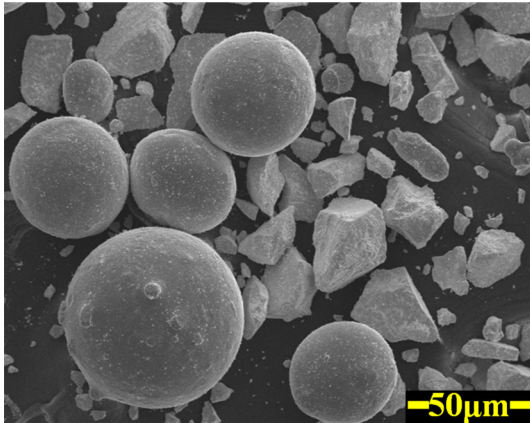


Fig. 1. Results of mixing Ta powder and Ni-based powder.

were determined before the coating was prepared; this layer had a high surface roughness and was subsequently machined to remove excess coating parts to obtain the required surface morphology. It is crucial to decrease the surface roughness of the coating and the machining allowance as well as to improve the performance of the coating. The surface morphology of the cladding layer and the three-dimensional morphology of the coating before and after remelting with different specific energies are shown in Fig. 2. Surface morphologies of the remelted coatings varied considerably with different laser specific energies. Figure 2a shows the surface morphology of the cladding layer without remelting. Although there were no obvious defects on the surface, there were several powder particles on the surface of the coating that were not completely melted, and this increased the surface roughness.

Figure 2b and c shows the 3D morphology of the cladding layer without laser remelting. There were many incompletely melted particles on the surface of the cladding layer, and the lap area between the cladding channels was obviously concave; moreover, the distance from the lowest to the highest part of the surface in Fig. 2b is smaller than that in Fig. 2c. The incompletely melted powder particles on the surface of the cladding layer may be attributed to several reasons: (1) the energy at the edge of the circular spot used for cladding may have been lower than that at the center, and because of the interaction between the laser and the alloy powder at the edge of the spot, some of the alloy powder may have not melted or melted incompletely, resulting in incompletely melted powder particles on the surface after the formation of the cladding layer; (2) as the

laser beam moved, the metal powder fell into the molten pool before the pool was completely solidified, and as the solidification proceeded, the incompletely melted particles appeared on the surface of the cladding layer.⁴⁶ The lap area of the cladding layer was concave because the energy at the edge of the circular laser spot was low and there was a small amount of molten alloy powder, which resulted in a single coating with a thin edge. A layer overlapped at $\sim 50\%$ of the width direction of the previous coating, which decreased the concave degree of the lap area; however, there was still some concave phenomenon. The distance from the lowest to the highest point of the surface in Fig. 2b was less than that in Fig. 2c because the cladding powder used in Fig. 2c was a mixture of Ni-based spherical powder and irregularly shaped Ta powder. During laser cladding, the irregularly shaped Ta powder influenced the fluidity and uniformity of powder feeding; as a result, the maximum height difference of the surface in Fig. 2c was greater than that in Fig. 2b.

To decrease the surface roughness and improve the performance of the composite coating with Ta powder, the coating surface was remelted with different specific energies. The remelting results are shown in Fig. 2d, e and f. The incompletely melted powder particles on the surface of the whole cladding layer disappeared after remelting, which decreased the surface roughness of each cladding layer. This was mainly because the surface of the cladding layer was scanned again using a laser beam with a different specific energy, which again melted some thickness of the cladding layer and the alloy powder particles on the surface. Moreover, no new powder was added between the melting of the coating and solidification of the melt pool. Consequently, the surface of the single coating was smoother after the formation of the cladding layer.

Analyzing Fig. 2d, e and f showed that the maximum height differences of the remelted coating surface were 148.594, 178.499, and 291.564 μm , respectively, and were smaller than 368.355 μm in Fig. 2c (the un-remelted composite coating). The maximum height difference of the remelted coating surface increased with the increase of the laser remelting specific energy. This was because as the specific energy of the laser increased, the thermal impact of the laser was enhanced. Moreover, the higher intensity of the thermal impact on the cladding layer increased the maximum height difference on its surface. During laser remelting, a

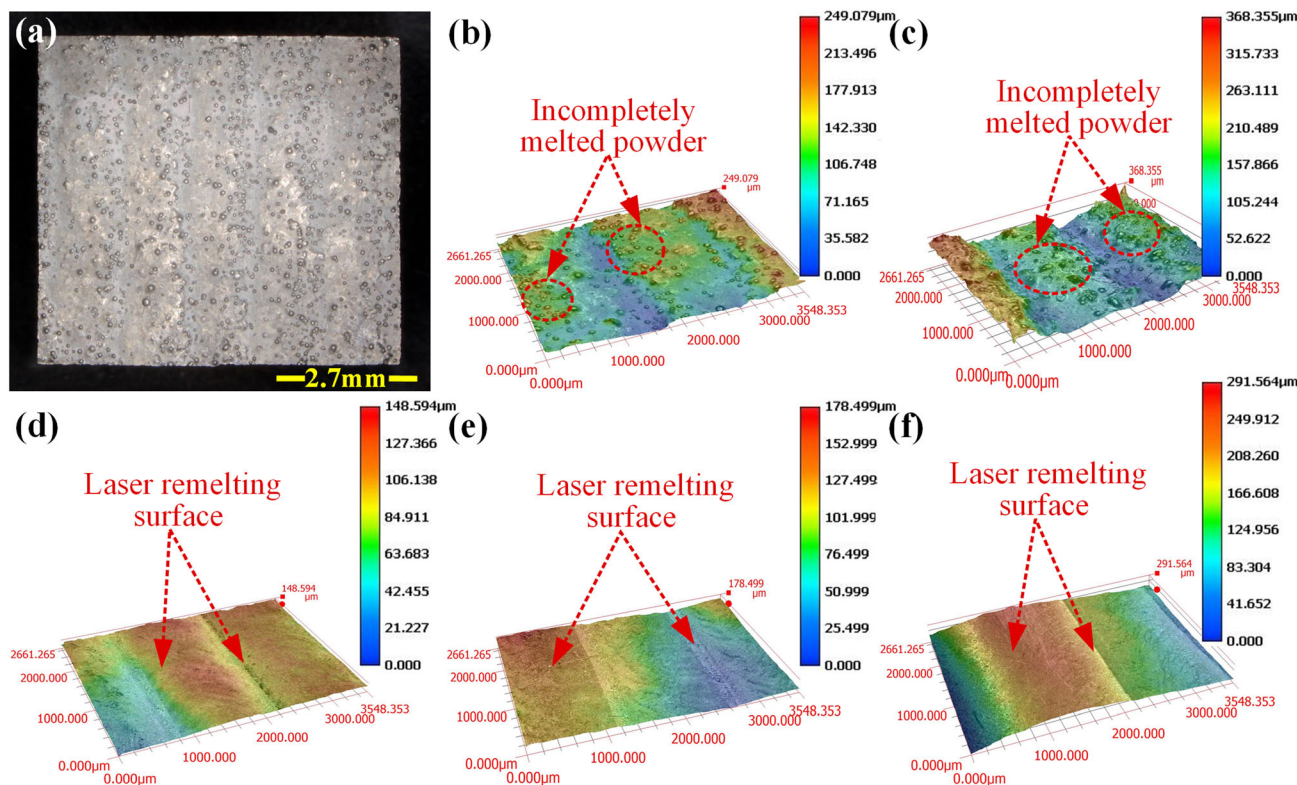


Fig. 2. Surface morphology of the cladding layer and 3D morphology of each cladding layer: (a) surface morphology of the cladding layer; (b)–(f) samples 1–5, respectively.

suitable laser specific energy should be selected to remelt the composite coating to eliminate incompletely melted alloy powder particles on the surface and effectively decrease the surface roughness. A very high remelting laser specific energy cannot achieve adequate surface roughness reduction of the composite coating, while a very small remelting laser specific energy cannot melt the incompletely melted particles. Therefore, a suitable remelting laser specific energy is essential for ensuring high-quality remelting. Thus, based on above findings, the surface quality of the cladding layer was considerably improved when the surface remelting specific energy of the Ni-based composite cladding layer was 20.83 J/mm^2 . Improved surface quality decreased the subsequent machining allowance, which can promote resource-saving and environmentally friendly manufacturing.

Phase Composition

During the remelting of a composite coating by a high-energy laser beam, complex chemical reactions occur in the melt pool.⁴⁷ The magnitude of the remelting specific energy influences the chemical reactions that occur on the surface, and it directly influences the phases generated in the coating. To study the phase composition of remelted composite coatings at different laser specific energies, physical phase analysis was carried out on remelted samples. Figure 3 shows the XRD analysis results of

composite cladding layers. As the specific energy of laser remelting increased, there was no significant change in the phase type of each remelted sample; however, the intensity of the diffraction peak was increased and then decreased. The intensity of the diffraction peak of sample 4 was the highest. It showed that the crystals of sample 4 were well developed and the content of formed phases were more. In the samples before and after laser remelting, the main phases were Ni, FeNi_3 , $\text{Cr}_{1.12}\text{Ni}_{2.88}$, and Cr_{23}C_6 . Therefore, the main species of the phases did not change after laser remelting.

Microstructure and EDS Analysis

The cladding layer was remelted with various specific energies, and the EDS line scanning results from the substrate to the top of the cladding layer on the section perpendicular to the cladding scanning direction are shown in Fig. 4. The elemental compositions in different positions of the cladding layer of each sample were different, but they all comprised Ni, Fe, Ta, C, and Si, among other elements. In samples 3–5, the elemental composition fluctuated at the interface between the matrix and the cladding layer, which was mainly attributed to the different types and contents of elements in the matrix and the cladding layer. In each remelted sample, after the concentration of Ta increased to a certain height through the interface, there was a large fluctuation in the cladding layer. After the

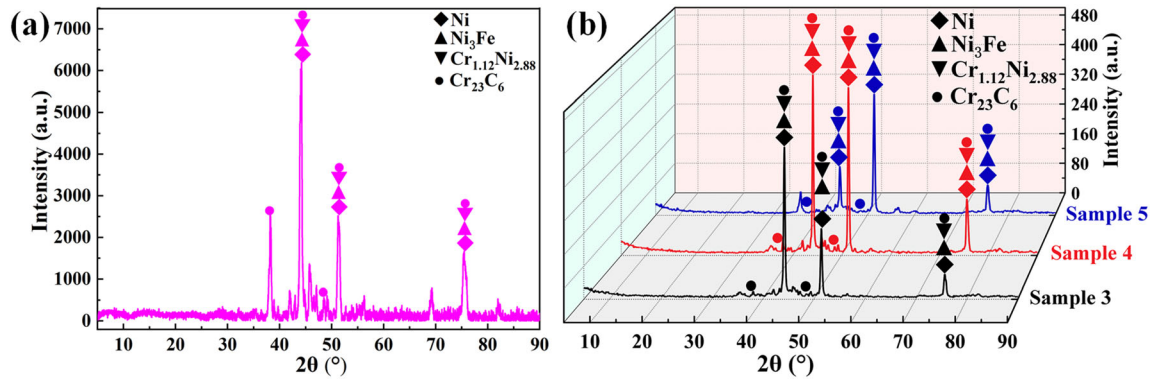


Fig. 3. XRD analysis results of samples: (a) sample 2; (b) samples 3–5.

concentration of Ni increased to a large extent through the interface, there was a small fluctuation around a certain concentration in the cladding layer. This was because the cladding layer contained more Ta and Ni, while the matrix material contained only a small amount of Ni and no Ta. As the specific energy of laser remelting increased, the Ta and Ni elemental curves transitioned more gently at the interface between the substrate and the cladding layer. This indicated that the cladding layer was remelted by a larger specific energy laser. The Ta and Ni at the bottom of the melt pool were more fully diffused by gravity and convection at the bonding interface between the substrate and the cladding layer, which effectively decreased the difference in chemical composition between the two sides of the bonding interface and facilitated the formation of a metallurgical bond between the coating and the substrate.⁴⁸

Analysis of the variation curves of Fe in Fig. 4a2–c2 showed that the matrix contained high concentrations of Fe, which fluctuated slightly. Moreover, at the junction of the matrix and the cladding layer, an overall rapid decreasing trend of Fe concentration was observed. The Fe content in Fig. 4b2 showed a very small rebound during the rapid decline before continuing to decrease rapidly and then stabilized at a relatively low level on the cladding layer. This was because the matrix material mainly contained Fe and the cladding layer contained relatively less Fe. This non-uniformity in Fe content caused the curve to fluctuate. Argon was used as a protective gas in the laser cladding process; as a result, O content in the matrix and the cladding layer did not change considerably. Analysis of the internal morphology of the cladding layer (Fig. 4) showed that as the laser remelting specific energy increased, there were considerably fewer pores in the cladding layer, with almost no obvious pores (Fig. 4c1). This was because a large laser remelting specific energy enabled sufficient melting in the cladding layer, decreased the viscosity of the melt pool, and retained the melt pool for a longer period of time, which allowed sufficient time for the pores in the melt pool to rise up and escape.⁴⁹

The cross-sectional morphology of the cladding layer in Fig. 4 shows that there were some areas where white substances gathered in the cladding layer. The distribution of elements in the white substance aggregation zone was observed using EDS line scan analysis on the cladding layer of sample 3 (Fig. 5). EDS line scanning passed through the area without white aggregates, the area with dense white aggregates, and the area with sparse white aggregates, in that order. The Ta and Si content showed a similar trend during the line scanning process and varied with the density of white aggregates and with higher Ta and Si content in the dense white aggregates. The Ta and Si content in the white aggregate was higher, and the Ta mixed in the cladding material was one of the main elements to form the white aggregate. This was mainly attributed to the preferential solidification of Ta—with a high melting point—in the molten pool, which promoted the formation of white aggregates. The elemental content of Ni and Fe also followed a similar trend, with the exception that Ni and Fe contents were higher in the absence of white aggregates and lower in the dense white aggregates than in the sparse ones. This indicated that the white aggregates contained relatively small amounts of Ni and Fe. Cr content was higher in the region without white aggregates, and it was lower and evenly distributed in the region with dense white aggregates. Furthermore, B, C, and O with low content were evenly distributed on the whole straight line scanned by EDS. Table III shows the results of the EDS point analyses for the dense and sparse white aggregates (Fig. 5). Ta content was highest in the two regions with different densities of white aggregates. With the thinning of white aggregates, Ta content decreased and Ni content increased. This trend was consistent with the results of EDS line scanning. The variation in the content of the other elements with sparse white aggregates was in general agreement with the results of the EDS line scan analyses, which further validated the results of the EDS line scan analysis.

Changes in specific energy laser remelting influenced the internal microstructure of the cladding

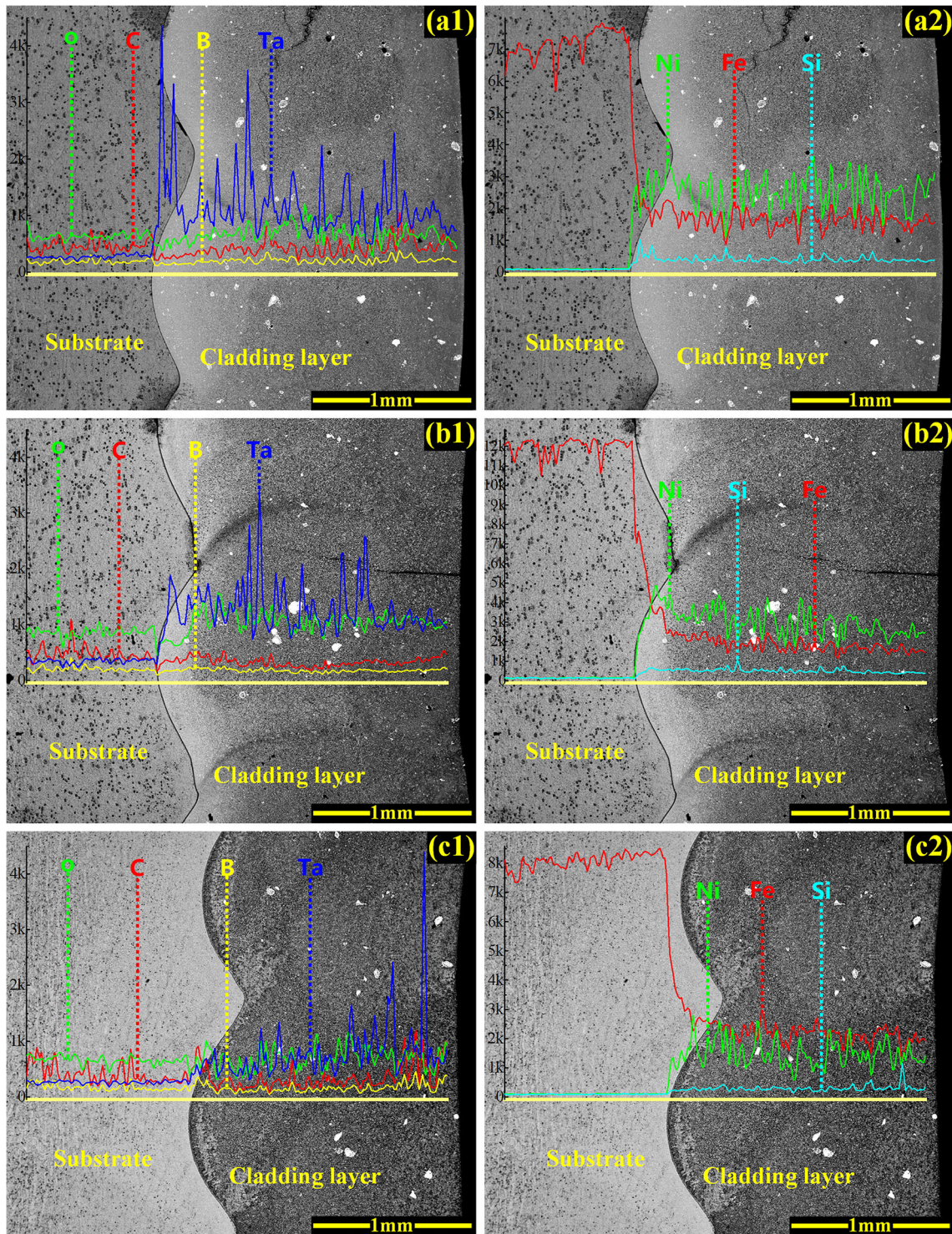


Fig. 4. EDS line scanning results from substrate to cladding layer after variable specific energy remelting and SEM analysis: (a1) and (a2) sample 3; (b1) and (b2) sample 4; (c1) and (c2) sample 5.

layer by influencing the temperature and solidification rate in the melt pool. The cross-sectional microstructure of the cladding layer before and after the specific energy remelting is illustrated in Fig. 6. Analysis of the microstructure diagrams of the upper, middle, and lower parts of the composite

coating before and after laser remelting with different specific energies showed that the crystal structure was dominated by fine dendrites and equiaxed crystals in the upper part of the cladding layer. The overall microstructure size of the upper part of the cladding layer was smaller than that of the middle

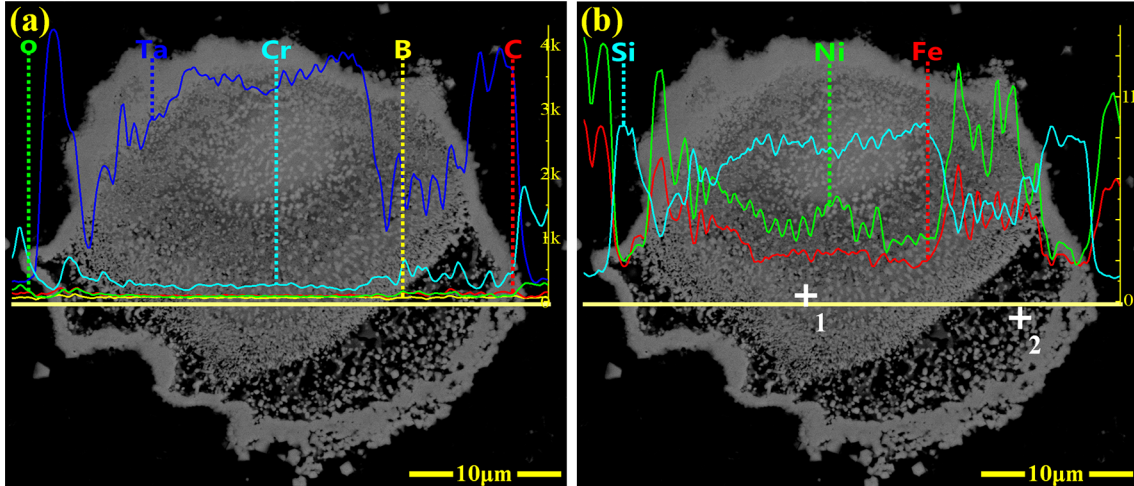


Fig. 5. EDS line scan results of the white matter aggregation area: (a) EDS line scan analysis; (b) EDS line scan analysis and spot analysis locations.

Table III. EDS point analysis results

Position	Element (wt.%)							Element (at.%)						
	C	O	Si	Cr	Fe	Ni	Ta	C	O	Si	Cr	Fe	Ni	Ta
1	6.43	1.45	4.14	1.86	2.94	8.37	74.80	-	-	-	-	-	-	-
2	9.60	0.97	6.27	2.72	3.08	20.07	57.29	-	-	-	-	-	-	-
A	11.18	1.56	-	6.65	3.11	1.81	75.70	56.04	5.86	-	7.70	3.36	1.85	25.19
B	12.51	3.13	1.16	14.50	7.41	4.14	57.16	50.15	9.43	1.99	13.43	6.39	3.40	15.21
C	13.30	1.66	-	11.07	2.66	2.38	68.94	58.50	5.47	-	11.25	2.52	2.14	20.13
D	10.27	1.17	-	9.65	2.62	2.53	73.76	53.05	4.54	-	11.52	2.91	2.68	25.30
E	6.34	-	0.22	47.05	35.65	10.73	-	23.34	-	0.35	40.01	28.22	8.08	-
F	0.41	0.57	2.69	6.63	20.83	68.86	-	1.87	1.95	5.20	6.93	20.27	63.77	-
G	10.04	2.47	4.36	6.53	18.49	58.12	-	32.25	5.96	5.99	4.84	12.77	38.20	-
H	11.62	3.09	1.05	13.69	5.39	3.34	61.81	49.44	9.88	1.92	13.46	4.93	2.91	17.46
I	10.19	0.79	-	7.02	2.35	2.86	76.79	54.83	3.18	-	8.72	2.72	3.15	27.41
J	5.87	-	0.15	48.05	35.04	10.89	-	21.91	-	0.24	41.42	28.12	8.32	-

and lower part. This was mainly because when the melt pool cooled, the upper part of the cladding layer dissipated heat through air medium via radiation and convection and matrix conduction, with small temperature gradients and fast solidification rates.^{50–52} Furthermore, a larger component subcooled to promote nucleation, and as a result, the upper part of the cladding layer had a finer grain microstructure. Figure 6b1–d1 shows that the overall grain size of the upper part of the cladding layer increased with increasing remelting specific energy. However, after remelting, in samples 3 and 4, the overall crystal size of the upper part of the cladding layer (Fig. 6b1 and c1) decreased to a significantly smaller value than that of the upper part of the unremelted cladding layer (Fig. 6a1). This was mainly because a larger laser remelting specific energy facilitated adequate crystal growth. The overall crystal size of the upper part of the cladding layer of samples 3 and 4 may also be because the remelting specific energies were much smaller than

the laser cladding specific energies. The remelting specific energy of sample 5 was closer to the cladding specific energy, and as a result, the overall grain size in the upper part of the cladding layer was larger at a laser remelting specific energy of 75 J/mm². As the distance from the upper part of the cladding layer increased, the temperature gradient at the front of the solid–liquid interface inside the cladding layer increased and the solidification rate decreased. In the middle of the cladding layer, the crystal growth rate was slower and a coarser crystal microstructure was formed than in the upper part.

Figure 6b2–d2 shows that the content of columnar crystals in the middle of the cladding layer gradually increased with increasing specific energy of laser remelting. The content of white structures in the middle of the cladding layer varied after remelting with different specific energies. The white structure content in Fig. 6b2 was significantly less than that in Fig. 6a2, indicating that a

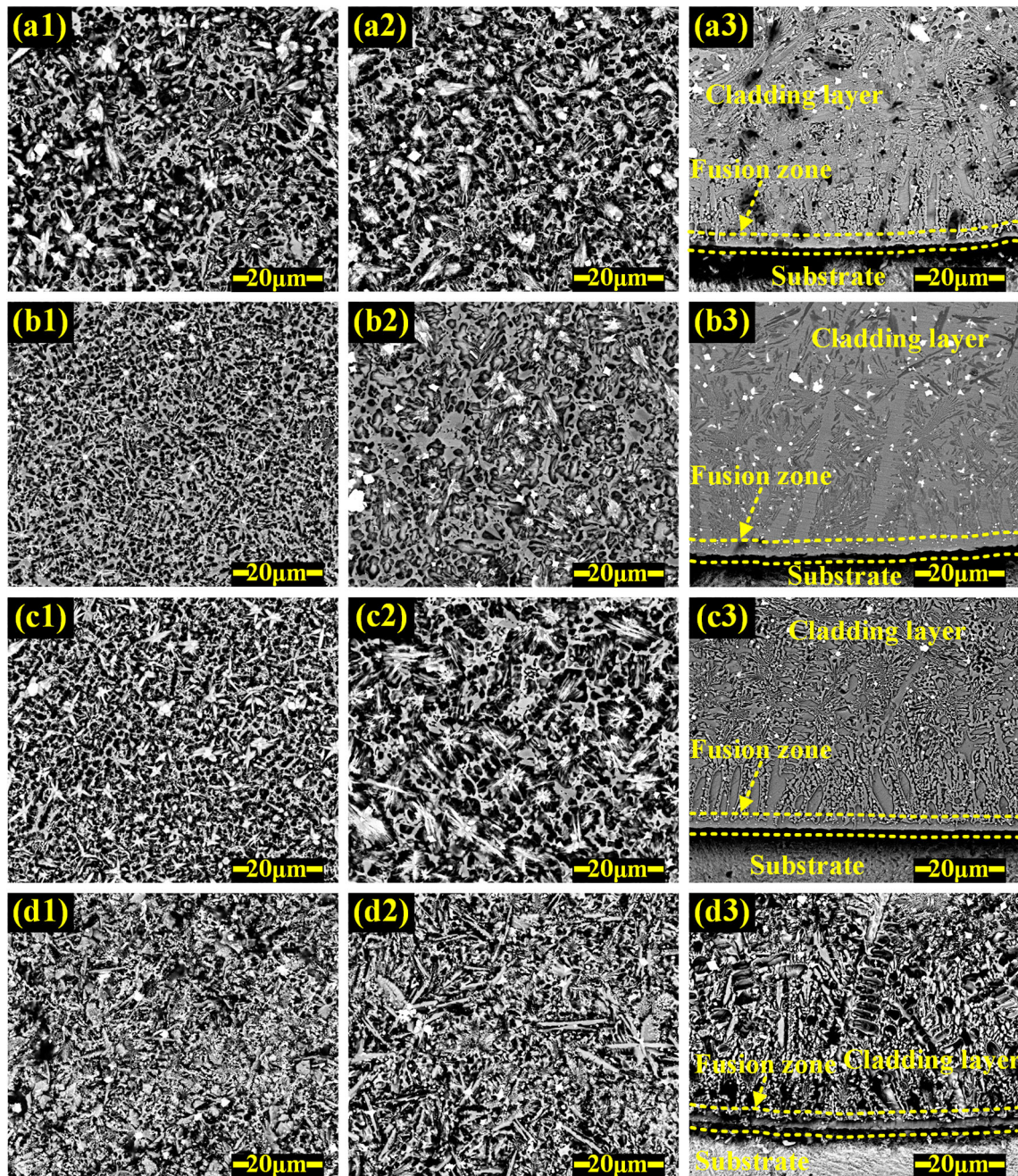


Fig. 6. Cross-sectional microstructure of the cladding layer before and after variable specific energy remelting: (a1)–(d1) upper part of the cladding layer of samples 2–5; (a2)–(d2) middle part of the cladding layer of samples 2–5; (a3)–(d3) lower part of the cladding layer of samples 2–5.

suitable remelting specific energy was conducive to the adequate dispersion of the white structures. Figure 6a3–d3 shows the microstructure of the lower part of the cladding layer, with the largest temperature gradient and the smallest solidification rate. A narrow and long banded structure was formed at the fusion interface between the substrate and the cladding layer. A well-formed banded structure in the fusion zone resulted in a better metallurgical bond between the matrix and the cladding layer. The banded structure existed in the

form of plane crystal. Analysis showed that the banded structure in Fig. 6c3 was the best formed after laser remelting of the cladding layer, while the banded structure in the lower part of the cladding layer prepared by other processes had different degrees of defects, especially the fracture of the banded structure in Fig. 6a3 and d3. Thus, the remelting specific energy considerably influenced the bonding between the substrate and the cladding layer. In the lower part of the molten pool, most of the heat was transmitted and dissipated through

the matrix, and very coarse columnar and dendritic crystals were formed that grew at an angle to the fusion line toward the top of the cladding layer. Furthermore, Fig. 6b3–d3 shows that with increase in laser remelting specific energy, the coarse dendrite near the fusion zone at the lower part of the cladding layer had an obvious thinning trend, but the overall crystal size first decreased and then increased, and the white bright color structure decreased. This was because after the cladding layer was remelted by the larger laser specific energy, the internal white bright color structure was decomposed, coupled with the convection and stirring effect of the molten pool,^{53,54} resulting in a white bright color structure that was more evenly distributed in the lower part of the cladding layer, and it promoted nucleation and grain refinement.⁴³ However, due to the different remelting specific energies on the thermal effect and cooling heat dissipation of the cladding layer, this led to the formation of partially coarse crystalline structures in the lower part of the cladding layer.

Figure 7 shows the EDS mapping results of B, C, Si, Cr, Fe, Ni, and Ta in the internal microstructure of the cladding layer after laser remelting. The white bright color was similar to the circular microstructure, which was rich in Si, Ta, and C. The corolliform microstructure and irregular microstructure were rich in Si, Cr, and other elements. The irregularly shaped dendrites in Fig. 7a had rounded white shiny microstructures at the initial end, but not on the corolliform microstructure. In some of the irregularly shaped dendrites, some directional growth was influenced by the circular white shiny microstructures. Thus, the circular white shiny microstructures hindered the direction of growth of some of the dendrites, and the mixing of Ta facilitated the strengthening of the fine crystals. This was because during the solidification of the melt pool, the high-melting-point phases of Ta or Ta carbides reached the solidification point first when the surrounding lower melting point material had not solidified. The first solidified phase promoted the formation of nuclei and

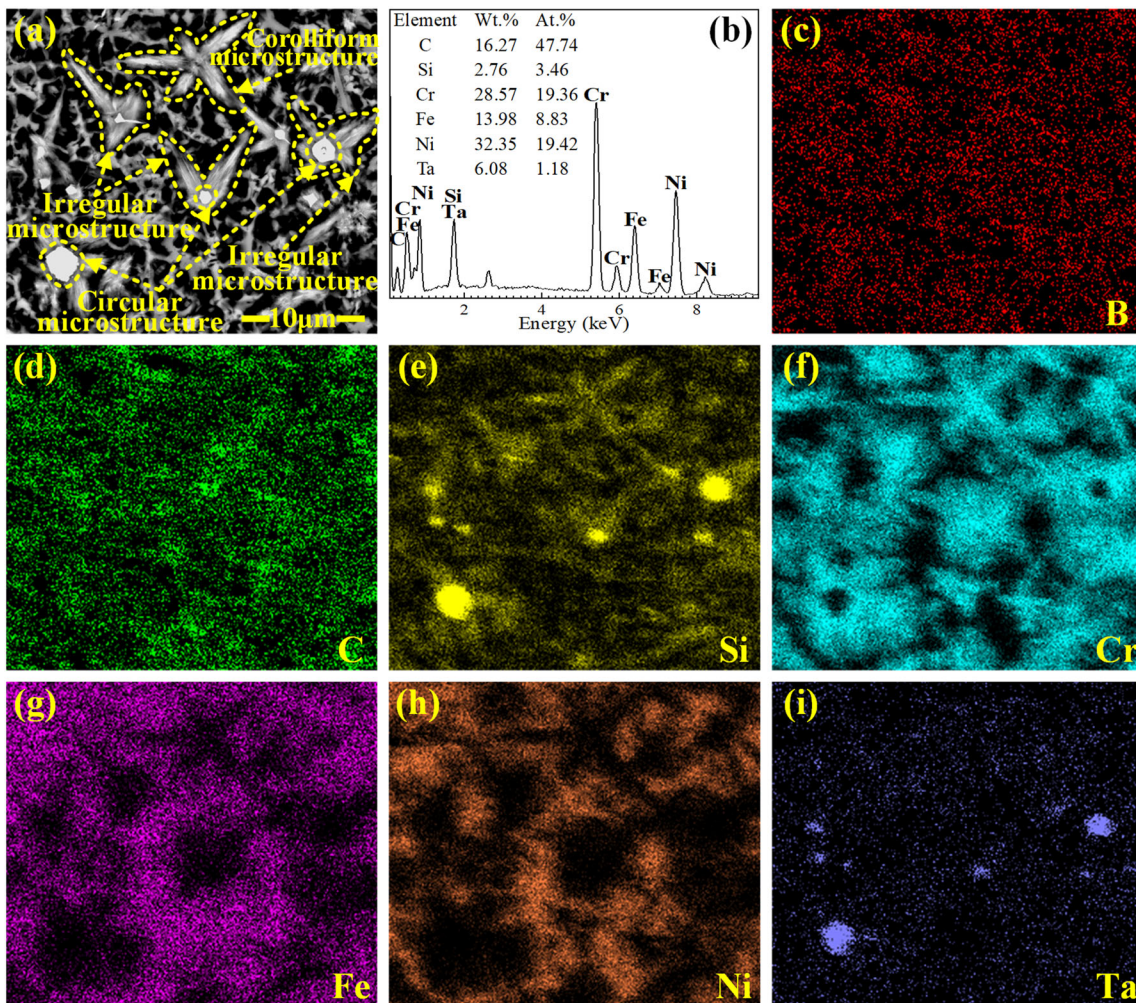


Fig. 7. EDS mapping results of the internal microstructure of the cladding layer: (a) scanning area; (b) EDS mapping elements; (c) B; (d) C; (e) Si; (f) Cr; (g) Fe; (h) Ni; (i) Ta.

hindered the growth of crystals. In addition, laser remelting reheated the cladding layer, which was conducive to more uniform dispersion of high-melting-point substances.

To study the elemental composition of different types of microstructures, EDS point analysis was carried out on the internal microstructure of the cladding layer (Fig. 8). The analysis results are shown in Table III. There were varying degrees of differences in the content of elements in different shapes of microstructures. The white bright block microstructure contained higher Ta content, while the long strip-like microstructure and the F region of the gray-black microstructure did not contain Ta. Ni was mainly enriched in the F region of the gray-black microstructure, while the relative content of Fe and Cr was significantly higher in the E and J regions of the crystal structure than in the other regions. This was mainly related to the elemental segregation formed by the rapid cooling of the melt pool under the influence of laser remelting. The G region mainly contained Fe, Ni, and C, while the F region mainly contained Fe, Ni, and Cr. Furthermore, the atomic ratio of Fe to Ni in both regions was approximately 1:3, and combined with the XRD analysis results, it was determined that FeNi_3 was formed in these two regions. The atomic ratio of Cr to C in the F region was close to 23:6, and in combination with XRD analysis results, it was determined that Cr_{23}C_6 was formed in this region. Ta and Cr are strong and medium-strong carbide-forming elements.⁵⁵ Because of the difference of electron saturation outside the nuclei of Ta and Cr atoms, the binding ability between Ta and C was stronger than that of Cr and C in the liquid molten pool. Thus, Ta formed carbides more easily than Cr. Thus, after variable specific energy laser remelting, the coating contained Cr carbides. Combined with contemporary literature findings,⁵⁵ it was determined that the remelting coating contained carbides of Ta. The atomic percentages of C in the Ta-containing microstructure determined by EDS were all two times higher than those of Ta. The higher

atomic percentages of C provided favorable conditions for the formation of Cr carbides.

Microhardness Characteristics

To study the microhardness distribution characteristics of variable specific energy laser remelting coatings, the microhardness variation from the surface of the cladding layer to the substrate was tested. The average of the hardness of the first 18 test points was taken as the average microhardness of the cladding layer. The results of microhardness test of each sample are shown in Fig. 9a. The microhardness of the cladding layer was much higher than that of the substrate for all five samples, and at different locations on the cladding layer, the microhardness fluctuated to some extent. The microhardness of the remelted Ni-based composite cladding layer was higher than that of the unremelted one within a certain distance from the surface of the cladding layer, and the microhardness of the unremelted Ni-based composite coating was higher than that of the Ni-based coating. In the bonding area between the substrate and the cladding layer, due to convection in this area in the molten pool, the elements in the cladding layer and substrate were exchanged and diffused. Coupled with the cooling effect of the bonding area, there was a relatively gentle downward trend in hardness from the cladding layer to the substrate. In the Ni-based composite coating with 6 wt.% Ta powder, the average microhardness increased by approximately 83.66 $\text{HV}_{0.2}$ compared to the coating without the Ta powder. The average microhardness of the Ni-based composite coatings again increased to varying degrees after remelting at variable specific energies, with the average microhardness of the composite coatings increasing and then decreasing with increasing remelting specific energy. Among the three remelted samples, remelted sample 4 had the highest average microhardness of approximately 650.17 $\text{HV}_{0.2}$, which was 2.07 times that of the substrate. There were two main reasons for the increase in microhardness of the Ni-based composite coating after laser remelting. One, selecting the appropriate laser specific energy for remelting Ni-based composite coatings, through rapid cooling to promote nucleation, significantly decreased the size of metal grains, increased the proportion of grain boundaries, and refined the role of grain strengthening composite coatings. Two, laser remelting using a suitable specific energy heated the composite coating again, and as a result, the metal carbide reinforcing phase in the composite coating was more uniformly distributed. Moreover, the more uniform distribution of the reinforcing phase also helped hinder the growth of the crystals. In addition, the increase in average microhardness was also closely related to the number of reinforcing phases (such as metal carbides) formed.

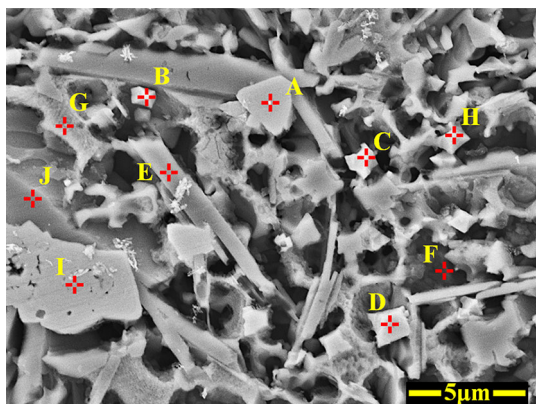


Fig. 8. EDS point analysis location.

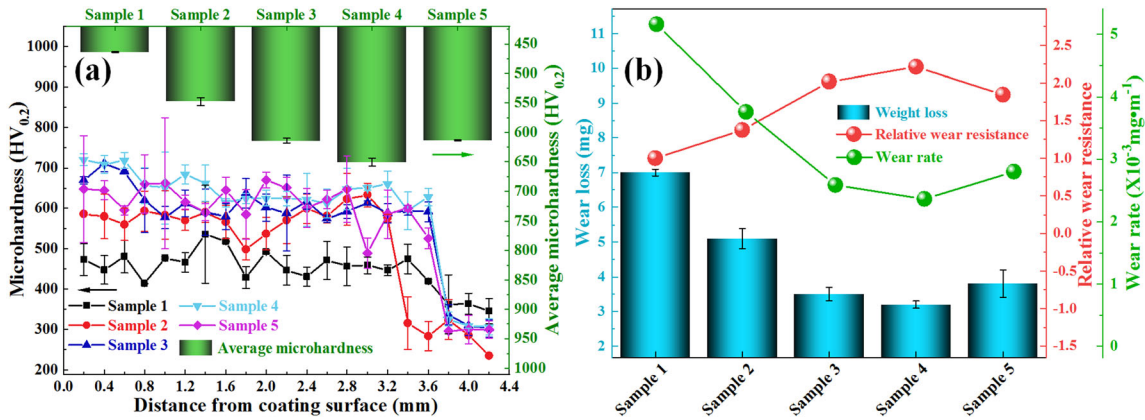


Fig. 9. Microhardness and wear resistance analysis: (a) microhardness of each sample; (b) analysis of the wear resistance of each sample.

Wear Resistance Analysis

To study the effect of various specific energy remelting values on the wear resistance of the composite coating, wear resistance tests were carried out on the cladding samples (Fig. 9b). Wear loss, wear rate (W), and relative wear resistance were used to characterize the wear resistance of the composite cladding layer. W represents the weight of wear loss per unit length, as shown in Eq. 2:⁵⁶

$$W = \frac{m}{\pi \cdot d \cdot n} \quad (2)$$

where d is the diameter of the wear pair, and n is the number of revolutions. Higher value of wear loss and wear rate implied poorer wear resistance and thereby better wear resistance. Compared to the unremelted samples, the wear resistance of the remelted samples improved to varying degrees. This was mainly due to the reduction of pores in the remelted layer and the more homogeneous dispersion of the reinforcing phase as well as the overall grain refinement. As the specific energy of the laser remelting increased, the wear loss and wear rate of the composite coating decreased and then increased. Sample 4 had the lowest wear loss and wear rate values. Thus, the wear resistance of the composite coating improved using the appropriate laser remelting specific energy. The relative wear resistance F was calculated using Eq. 3:^{47,57}

$$F = \frac{m_0}{m} \quad (3)$$

where m_0 denotes the average wear weight of sample 1, and m denotes the average weight loss of each sample. Among the five samples, the relative wear resistance value increased and then decreased in ascending order of sample number. Sample 4 had the highest relative abrasion resistance, indicating that the relative abrasion resistance of sample 4 was better than that of the other samples.⁵⁸ In combination with the average microhardness characteristics of the cladding layer, it was determined that as the specific energy of laser remelting

increased, the relative wear resistance value of the cladding layer and the average microhardness showed a positive correlation.

CONCLUSION

To improve the surface quality and performance of laser cladded Ni-based coatings, in this study, we conducted an investigation on the cladding material as well as the remelting process. Remelting of Ta/Ni-based composite laser cladding layers was carried out using different laser specific energies. The effects of different laser remelting specific energies on the surface morphology, phase composition, microstructure, element distribution, and mechanical properties of the cladding layers were investigated, and the changes in the mechanical properties of Ni-based cladding layers before and after the addition of Ta elements were compared. The main conclusions of the study are as follows.

- (1) After remelting with three values of laser specific energies, the unmelted powder particles on the surface of the cladding layer disappeared, effectively reducing the surface roughness of each cladding layer. The maximum height difference on the surface of the remelted layer increased with increase in laser specific energy. However, it was smaller than the maximum height difference on the surface of the un-remelted composite coating. Moreover, the surface quality of the remelted layer with a laser specific energy of 20.83 J/mm^2 was relatively good.
- (2) With increase in the remelting specific energy, there were fewer internal pores in the cladding layer. A relatively large remelting specific energy facilitated the diffusion of Ta and Ni at the bonding interface between the substrate and the cladding layer, decreasing the difference in chemical composition between the two sides of the bonding interface. Sample 4 had better bonding between the cladding layer and the substrate, and the bonding interface

- existed in the form of a plane crystal.
- (3) A suitable value of remelting laser specific energy significantly decreased the grain size of the Ta/Ni-based composite coating. As the remelting specific energy increased, the overall grain size of the upper part of the composite coating gradually increased, the content of the central columnar crystal gradually increased, and the overall crystal size of the lower part first decreased and then increased. The bright white microstructure with a higher concentration of Ta hindered crystal growth.
 - (4) The average microhardness of the Ta/Ni-based composite remelted layer was higher than that before remelting, reaching approximately 650.17 HV_{0.2}, which was 2.07 times higher than that of the matrix. The wear resistance of the composite remelted layer also improved, first increasing and then decreasing with increase in remelting specific energy; there was a positive correlation between the average microhardness and the wear resistance.

ACKNOWLEDGEMENTS

The authors acknowledge the support to this work from the Key Laboratory Open Fund of Xinjiang Autonomous Region (2020520002), Research and Innovation Project of Xinjiang Autonomous Region (XJ2022G011), the University Science Research Planning Project of Xinjiang Autonomous Region (XJEDU2021Y008), Xinjiang Autonomous Region Fund Project (2021D01C103), and Research Fund of Xinjiang Institute of Engineering (2019xgy152112).

CONFLICT OF INTEREST

The authors declare that they have no known competing financial interests or personal relationships that could have appeared to influence the work reported in this paper.

REFERENCES

1. H. Zheng, M. Cong, D. Liu, H. Dong, and Y. Liu, *Int. J. Adv. Manuf. Technol.* 100, 599 (2019).
2. L. Zhu, P. Xue, Q. Lan, G. Meng, Y. Ren, Z. Yang, P. Xu, and Z. Liu, *Opt. Laser Technol.* 138, 106915 (2021).
3. G.A. Farotade, A.P.I. Popoola, and S.L. Pityana, *Surf. Rev. Lett.* 25, 1950005 (2018).
4. Y. Cai, Z. Luo, M. Feng, Z. Liu, Z. Huang, and Y. Zeng, *Surf. Coat. Technol.* 291, 222 (2016).
5. Q. Wang, Q. Li, L. Zhang, D.X. Chen, H. Jin, J.D. Li, J.W. Zhang, and C.Y. Ban, *Ceram. Int.* 48, 7905 (2022).
6. Z. Gao, H. Ren, Y. Yuan, Z. Gao, E. Liu, and C. Zhang, *Micron* 150, 103146 (2021).
7. R. Li, Z. Li, J. Huang, and Y. Zhu, *Appl. Surf. Sci.* 258, 7956 (2012).
8. N.L. Do Vale, C.A. Fernandes, R.A. de Santos, T.F.A. Santos, S.L. Urtiga Filho *JOM* 73, 2868 (2021).
9. H. Liu, X. Du, H. Guo, J. Liu, P. Chen, H. Yang, and J. Hao, *Optik* 228, 166194 (2021).
10. Y. Jia, W. Sun, and K. Wang, *WSRJ* 6, 8 (2020).
11. C. Cui, M. Wu, X. Miao, Y. Gong, and Z. Zhao, *J. Mater. Res. Technol.* 15, 2405 (2021).
12. X. Lei, C. Huajun, L. Hailong, and Z. Yubo, *Int. J. Adv. Manuf. Technol.* 90, 1383 (2017).
13. F. Weng, C. Chen, and H. Yu, *Mater. Des.* 58, 412 (2014).
14. W. Yuan, R. Li, Z. Chen, J. Gu, and Y. Tian, *Surf. Coat. Technol.* 405, 126582 (2021).
15. G. Singh, M. Kaur, and R. Upadhyaya, *J. Therm. Spray Technol.* 28, 1081 (2019).
16. Y. Cao, N. Farouk, M. Taheri, A.V. Yumashev, S.F.K. Bozorg, and O.O. Ojo, *Surf. Coat. Technol.* 412, 127010 (2021).
17. T. Yu, J. Chen, Y. Wen, and Q. Deng, *Appl. Surf. Sci.* 547, 149171 (2021).
18. Z. Yu, L. Li, D. Zhang, G. Shi, G. Yang, Z. Xu, and Z. Zhang, *Chin. J. Mech. Eng.* 34, 92 (2021).
19. Z. Zhang, Y. Zhao, Y. Chen, Z. Su, J. Shan, A. Wu, Y.S. Sato, H. Gu, and X. Tang, *Mater. Des.* 198, 109346 (2021).
20. F. Fu, Y. Zhang, G. Chang, and J. Dai, *Optik* 127, 200 (2016).
21. J. Ning, D.E. Sievers, H. Garmestani, and S.Y. Liang, *J. Manuf. Process.* 49, 135 (2020).
22. C. Guo, J. Zhou, J. Zhao, L. Wang, Y. Yu, J. Chen, and H. Zhou, *Tribol. Lett.* 44, 187 (2011).
23. X. Zhang, X. Cui, G. Jin, Q. Ding, D. Zhang, X. Wen, L. Jiang, S. Wan, and H. Tian, *J. Alloys Compd.* 891, 161756 (2022).
24. A. Farnia, F. MalekGhaini, J.C. Rao, V. Ocelik, and J.T.M. De Hosson, *Surf. Coat. Technol.* 213, 278 (2012).
25. G. Jiang, C. Cui, L. Chen, Y. Wu, and X. Cui, *Materials* 14, 7437 (2021).
26. Z. Shengbin, J. Chenpeng, Y. Yuxue, W. Lixin, H. Yiming, and Y. Lijun, *J. Alloys Compd.* 908, 164612 (2022).
27. Y. Zhao, K. Feng, C. Shen, and Z. Li, *Mater. Lett.* 257, 126614 (2019).
28. J. Lei, C. Shi, S. Zhou, Z. Gu, and L.-C. Zhang, *Surf. Coat. Technol.* 334, 274 (2018).
29. A. Iqbal, G. Zhao, H. Suhaimi, N. He, G. Hussain, and W. Zhao, *Int. J. Adv. Manuf. Technol.* 111, 2475 (2020).
30. J.M. Flynn, A. Shokrani, S.T. Newman, and V. Dhokia, *Int. J. Mach. Tools Manuf.* 101, 79 (2016).
31. J.L. Dávila, P.I. Neto, P.Y. Noritomi, R.T. Coelho, and J.V.L. da Silva, *Int. J. Adv. Manuf. Technol.* 110, 3377 (2020).
32. U.M. Dilberoglu, B. Gharehpapagh, U. Yaman, and M. Dolen, *Int. J. Adv. Manuf. Technol.* 113, 623 (2021).
33. G. Zeng, S.H. Zahiri, S. Gulizia, Y. Chen, X.-B. Chen, and I. Cole, *J. Mater. Res.* 36, 3679 (2021).
34. L. Li, A. Haghghi, and Y. Yang, *J. Manuf. Process.* 33, 150 (2018).
35. Y. Cai, Y. Cui, L. Zhu, R. Tian, K. Geng, H. Li, and J. Han, *Surf. Eng.* 37, 1496 (2021).
36. X. Xu, J.L. Du, K.Y. Luo, M.X. Peng, F. Xing, L.J. Wu, and J.Z. Lu, *Surf. Coat. Technol.* 422, 127500 (2021).
37. S. Zhou, Y. Xu, B. Liao, Y. Sun, X. Dai, J. Yang, and Z. Li, *Opt. Laser Technol.* 103, 8 (2018).
38. D. Cong, H. Zhou, Z. Ren, Z. Zhang, H. Zhang, C. Meng, and C. Wang, *Mater. Des.* 55, 597 (2014).
39. B. Das, M. Gopinath, A.K. Nath, and P.P. Bandyopadhyay, *Optik* 227, 166030 (2021).
40. B. Xin, X. Zhou, G. Cheng, J. Yao, and Y. Gong, *Opt. Laser Technol.* 127, 106087 (2020).
41. Z. Kuai, Z. Li, B. Liu, W. Liu, and S. Yang, *Mater. Chem. Phys.* 285, 125901 (2022).
42. H. Wang, Y. Cheng, J. Yang, and Q. Wang, *Surf. Coat. Technol.* 414, 127081 (2021).
43. T. Han, Y. Liu, M. Liao, D. Yang, N. Qu, Z. Lai, and J. Zhu, *J. Mater. Sci. Technol.* 99, 18 (2022).
44. S. Zhou, J. Lei, X. Dai, J. Guo, Z. Gu, and H. Pan, *Int. J. Refract. Met. Hard Mater.* 60, 17 (2016).
45. P. Fan and G. Zhang, *Int. J. Refract. Met. Hard Mater.* 87, 105133 (2020).
46. W. Xi, B. Song, Z. Wang, T. Yu, J. Wang, and Y. Dai, *Surf. Coat. Technol.* 408, 126789 (2021).
47. K. Wang, D. Du, G. Liu, B. Chang, J. Ju, S. Sun, and H. Fu, *J. Alloys Compd.* 802, 373 (2019).
48. D. Shang, J. Zhang, A. Feng, Y. Zhou, J. Tang, and F. Chen, *Chin. J. Lasers* 47, 0902004 (2020).

49. Y. Li, S. Dong, S. Yan, X. Liu, E. Li, P. He, and B. Xu, *Opt. Laser Technol.* 112, 30 (2019).
50. K. Huo, J. Zhou, F. Dai, and J. Xu, *Appl. Surf. Sci.* 545, 149078 (2021).
51. Y. Huang, X. Zeng, Q. Hu, and S. Zhou, *Appl. Surf. Sci.* 255, 3940 (2009).
52. Y. Shi, Y. Li, J. Liu, and Z. Yuan, *Opt. Laser Technol.* 99, 256 (2018).
53. Y. Jiang, Y. Cheng, X. Zhang, J. Yang, X. Yang, and Z. Cheng, *Optik* 203, 164044 (2020).
54. S. Sun, H. Fu, X. Ping, J. Lin, Y. Lei, W. Wu, and J. Zhou, *Appl. Surf. Sci.* 455, 160 (2018).
55. T. Yu, Q. Deng, G. Dong, and J. Yang, *Appl. Surf. Sci.* 257, 5098 (2011).
56. Q. Xiao, W. Lei Sun, K. Xin Yang, X. Feng Xing, Z. Hao Chen, H. Nan Zhou, and J. Lu, *Surf. Coat. Technol.* 420, 127341 (2021).
57. L. Xu, J. Xing, S. Wei, Y. Zhang, and R. Long, *Wear* 262, 253 (2007).
58. W. Kaiming, L. Yulong, F. Hanguang, L. Yongping, S. Zhenqing, and M. Pengfei, *Surf. Eng.* 34, 267 (2018).

Publisher's Note Springer Nature remains neutral with regard to jurisdictional claims in published maps and institutional affiliations.

Springer Nature or its licensor (e.g. a society or other partner) holds exclusive rights to this article under a publishing agreement with the author(s) or other rightsholder(s); author self-archiving of the accepted manuscript version of this article is solely governed by the terms of such publishing agreement and applicable law.